Migration of Mg in Na-O-Mg Configuration for

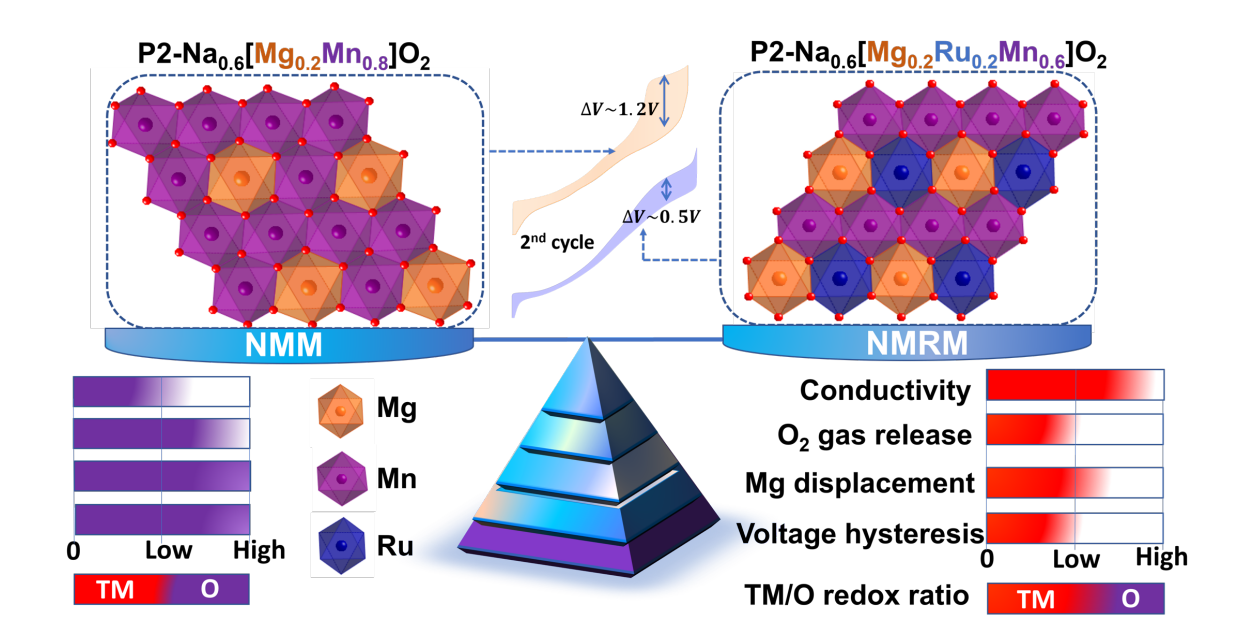
Oxygen Redox of Sodium Cathode

Jun Ho Yu, Natalia Voronina, Najma Yaqoob, Sungkyu Kim, Anil Kumar Paidi, Docheon Ahn, Kyuwook Ihm, Keun Hwa Chae, Min-Gi Jeong, Hun-Gi Jung, Olivier Guillon, Payam Kaghazchi,* Seung-Taek Myung*

Abstract

The effect of the 4d Ru element in P2-Na_{0.6}[Mg_{0.2}Ru_{0.2}Mn_{0.6}]O₂ is investigated. Ru-free Na_{0.6}[Mg_{0.2}Mn_{0.8}]O₂ is activated with the Mn³⁺/Mn⁴⁺ redox, after which the charge is compensated by the sluggish oxidation of lattice oxygen (O²⁻) to O₂ⁿ⁻ triggered by O₂ evolution from the oxide lattice. These effects are generally unfavorable and result in poor long-term cycle stability induced by the irreversible migration of Mg²⁺ from the transition metal (TM) to Na layers in the P2 structural framework. Benefiting from the covalent Ru bonded with O in the TM layers, the Mg migration reversibly progresses from the TM to sodium slabs without O₂ evolution in the structure. The associated reaction progresses via the active Mn⁴⁺/Mn³⁺ and O²⁻/(O₂)ⁿ⁻ reaction in addition to the Ru⁵⁺/Ru⁴⁺/Ru³⁺ redox pairs, endorsing the capacity increase (~210 mAh g⁻¹), with ~72.1% retention for 300 cycles.

TOC GRAPHICS



Mn-based P2-Na_x[Li_yTM_{1-y}]O₂ cathode materials are available to reach high capacity through the combination of cationic and anionic redox in Na cells.¹⁻¹¹ The Na–O–Li configuration induces the delivery of additional capacity assisted by the oxidation of oxygen when lone-pair electrons are formed in the O 2*p* orbital, provided that at least one of the following conditions is satisfied: 1) lattice oxygen evolution^{10,11} or 2) migration of the Li element to Na layers although the corresponding charge transfer is kinetically sluggish.^{10,12} The reaction is not limited to compounds that have alkali ions in the TM layer but is also available with divalent ions; namely, the presence of Mg in the TM layer, ^{13–17} P2-Na_x[Mg_yMn_{1-y}]O₂ (x = ~2/3, y = ~0.28). Recently, Grey et al.¹⁶ and Bruce et al.¹⁵ evaluated the mobility of Mg from TM to Na layers via Na – nuclear magnetic resonance (NMR), extended X-ray absorption fine structure (EXAFS) analysis, and density functional theory (DFT) calculation. This effect produces unpaired electrons in the O 2*p* orbital of lattice oxygen, enabling oxidation of the oxygen. Similarly, the presence of vacancies in the TM layers improved the electrode performance for P2-Na₂₆[Mg_{0.143}□_{0.036}Mn_{0.82}]O₂¹⁸ or P2-Na_{2/3}[Mg_{1/9}□_{1/9}Mn_{7/9}]O₂¹⁹.

Herein, we investigated P2-Na_{0.6}[Mg_{0.2}Mn_{0.8}]O₂ (Mn: 3.75+) by replacing part of the Mn with Ru element, P2-Na_{0.6}[Mg_{0.2}Ru_{0.2}Mn_{0.6}]O₂ (Mn: 3.67+ and Ru: 4+), to stabilize the electrode performance with improved reversibility. The introduced covalent Ru–O bond may share its character with oxygen that bonds with Mg and Mn in the TM layers.²⁰ As-synthesized Na_{0.6}[Mg_{0.2}Mn_{0.8}]O₂ (NMM) and Na_{0.6}[Mg_{0.2}Ru_{0.2}Mn_{0.6}]O₂ (NMRM) powders were refined with *P6₃/mmc* space group (see **Figure S1, S2, Table S1-S3**). The average oxidation state of Mn was slightly reduced with the introduction of Ru in Na_{0.6}[Mg_{0.2}Ru_{0.2}Mn_{0.6}]O₂ (~3.75 + for NMM and ~3.66+ for NMRM). The presence of Ru⁴⁺ renders more formation of Mn³⁺ in Na_{0.6}[Mg_{0.2}Ru_{0.2}Mn_{0.6}]O₂ for charge compensation. From this viewpoint, it is reasonable to consider from the increase in both the *α*- and *c*-axis in Na_{0.6}[Mg_{0.2}Ru_{0.2}Mn_{0.6}]O₂ that the formation of Mn³⁺ through replacing Mn⁴⁺ with Ru⁴⁺ in the TM layers is responsible for the lattice expansion owing to the relation of ionic radii among Mn³⁺ (0.72 Å), Mn⁴⁺ (0.67 Å), and

Ru⁴⁺ (0.76 Å). Benefitting from the electro-conducting character of Ru, the electric conductivity, measured by a four-probe method, was improved from 8.9×10^{-5} S cm⁻¹ (NMM) to 1.7×10^{-4} S cm⁻¹ (NMRM). Details of powder properties are described in **Figure S1-S3**, and **Table S1-S5**.

The first charge curve of the NMM electrode consists of two distinct processes at 0.1C (26 mA g⁻¹): a sharp voltage rise accompanied by ~0.2 mol of Na⁺ deintercalation in the voltage range of 2.65-4.2 V followed by a flat voltage plateau over 4.2 V with ~0.3 mol of Na⁺ deintercalation (Figure 1a). In consideration of the redox potential, it is most likely that the low-voltage process is related to Mn³+/Mn⁴+ charge compensation; however, the high-voltage plateau originated from oxidation of lattice oxygen. The corresponding discharge emerged with a stair-like voltage profile with two distinct regions: 3.5-2.5 V and 2.5-1.5 V, delivering a discharge capacity of ~204 mAh g⁻¹ with a large hysteresis in the operation voltage between charge and discharge. The oxidized species are reduced during discharge. For the NMRM electrode (Figure 1b), a similar tendency was observed; however, a more gradual voltage rise was observed with a decreased operation voltage of the high-voltage plateau. Such a gradual curve at low voltage can be caused by the oxidation of both Mn and Ru. In addition, a smaller portion of oxidation of oxygen would participate in the charge process. The total delivered capacity on charge was ~122 mAh g⁻¹, which corresponds to ~0.49 mol of extracted Na per formula unit. The discharge profile was also somewhat altered by the presence of Ru in NMRM. There was a clear rise of operation voltage in the voltage range of 4-2.5 V, and the profile became smoothened with reduced voltage hysteresis. The delivered discharge capacity was ~210 mAh g⁻¹. It is evident that Ru-replaced NMRM improves the cycling stability for 300 cycles (namely, 72.1% retention) compared to 27.7% for NMM (Figure S4a). The rate capability was measured up to 7C (1820 mA g⁻¹) (**Figure S4 b-d**). The Ru-replaced NMRM electrode had a discharge capacity of 122.1 mAh g⁻¹ at 7C. As mentioned in Figure S1, the improved electric conductivity for the Ru-replaced NMRM $(1.7 \times 10^{-4} \text{ S cm}^{-1})$ is thought to be the main factor resulting in the delivery of high capacity at high rates, compared to the value for the Ru-free NMM $(8.9 \times 10^{-5} \text{ S cm}^{-1})$.

To investigate the difference in the charge and discharge profiles for NMM and NMRM electrodes, *operando* XRD (*o*-XRD) analysis was performed during the initial 2 cycles in the voltage range of 1.5–4.5 V (**Figure 1c, 1d, and S5**). The findings demonstrate that the presence of Ru in the TM layers induced different structural evolution during electrochemical cycling, namely, maintenance of the P2 phase *via* solid-solution behavior for the NMM electrode (**Figure 1c and S5a**) and a reversible P2–OP4–P2/P'2 phase transformation for the NMRM cathode (**Figure S5b**). The details of the structural evolution and the corresponding variations in lattice parameters are described and presented in **Figure 1e, 1f and S5**. The difference in phase transformations in NMM and NMRM are related to the presence of the covalent character introduced by the Ru–O bond in the TM layers, as evidenced from the decrease in the *c*-axis parameter in the desodiated state, $0.4 \le x \le 0.2$ in Na₈[Mg_{0.2}Ru_{0.2}Mn_{0.6}]O₂ (**Figure 1f**).

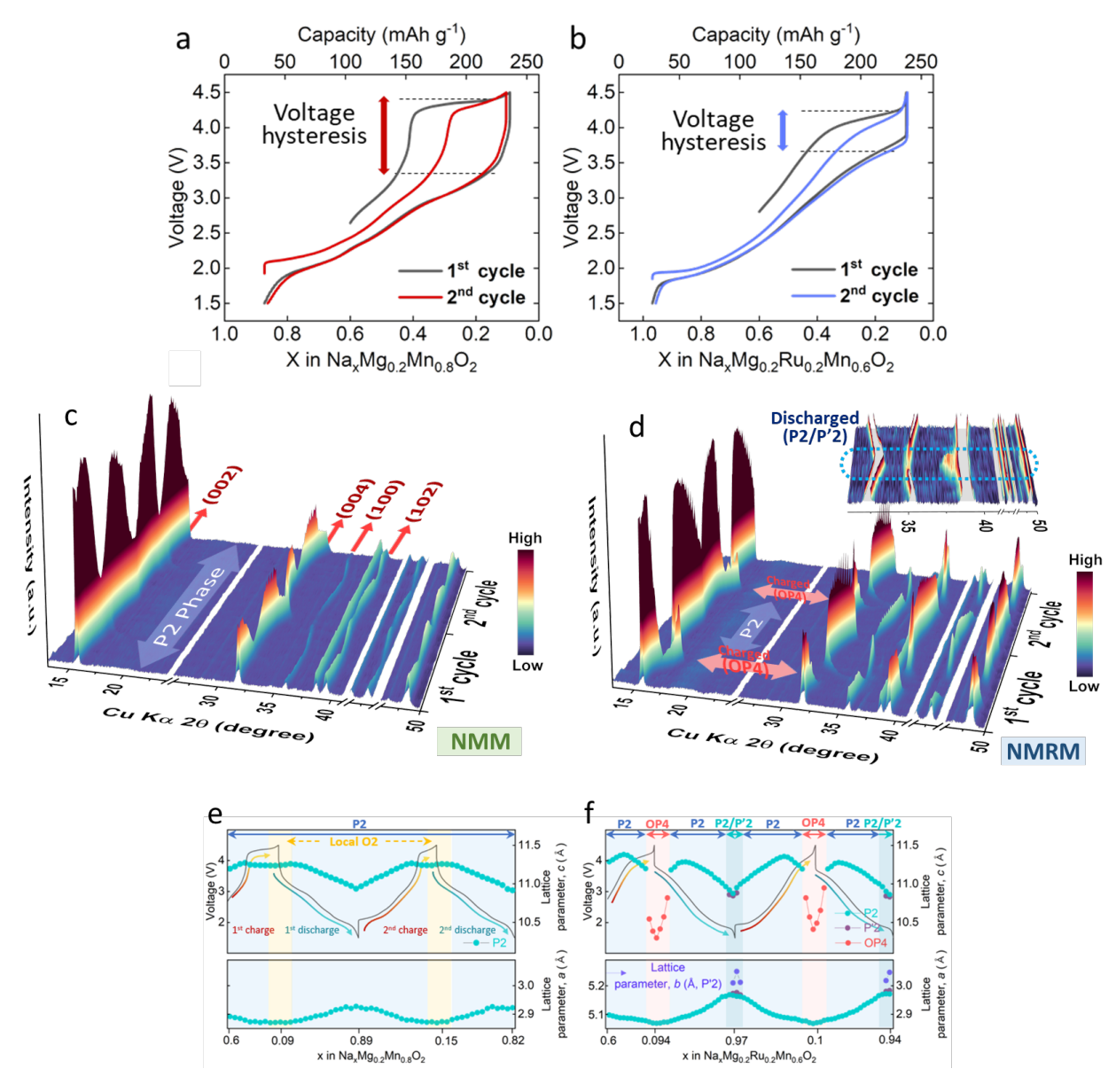


Figure 1. Voltage curves of (a) NMM and (b) NMRM electrodes. *Operando*-XRD patterns of (c) NMM and (d) NMRM. Voltage profile and corresponding lattice parameters of (e) NMM and (f) NMRM.

We conducted ex-situ X-ray absorption spectroscopy (XAS) studies for fresh, fully charged, and fully discharged electrodes (Figure 2). Mn with the average oxidation of 3.75+ was oxidized to 4+ (close to the reference $Mn^{4+}O_2$) at 4.2 V (x = 0.4 in $Na_x[Mg_{0.2}Mn_{0.8}]O_2$, Figure 2a and S6). However, there were negligible changes in the X-ray absorption near edge spectroscopy (XANES) spectrum after charging to 4.5 V in comparison to the spectrum observed at 4.2 V, indicating the inactivity of Mn⁴⁺ on the high-voltage plateau over 4.2 V. This finding agrees with the variation of the a-axis parameter shown in **Figure 1e**. That is, the a-axis parameter increased to 4.2 V (x = 0.4 in Na_x[Mg_{0.2}Mn_{0.8}]O₂) due to the oxidation of Mn toward Mn^{4+} , whereas the inactivity of Mn over 4.2 V led to the negligible change in the a-axis parameter on charge. During discharge, the Mn K-edge spectrum showed almost no shift to lower photon energy to 3.0 V (x = 0.4 in $Na_x[Mg_{0.2}Mn_{0.8}]O_2$). Further sodiation, however, resulted in a major shift at 1.5 V, reaching an average oxidation state of Mn of ~3.35+ (Figure 2a and S6). Similarly, for the NMRM electrode, Mn^{3.66+} in the fresh state was active upon charging to 4.0 V, showing a visible shift toward Mn⁴⁺, with no further change in the spectra over 4V plateau (Figure 2b and S7). Despite the reduction of Mn on discharge, the NMRM electrode exhibited similar reduction of Mn toward ~Mn 3.4+ in the fully discharge state (1.5 V). In addition, turning to the Ru K-edge spectra, there is a visible shift of ~0.2 eV toward the higher-energy region during the first charge (**Figure 2c**), as Ru⁴⁺ participated in the oxidation process toward Ru⁵⁺, though slightly, in this operation range. Surprisingly, the spectra moved toward lower energy much more (~ 1.6 eV) on discharge to 1.5 V (Figure 2c), indicating reduction of Ru⁵⁺ to Ru⁴⁺ and even to Ru³⁺. The Ru⁵⁺/Ru⁴⁺/Ru³⁺ redox was also active in the second cycle (Figure 2d).

According to the extended X-ray absorption fine structure (EXAFS) spectra of Mn (**Figure 2e**), the Mn–O and Mn–M distances decreased to 4.2 V (x = 0.4 in Na_x[Mg_{0.2}Mn_{0.8}]O₂); however, not much changed during further charging to 4.5V. This result is consistent with the *operando* XRD results (**Figure 1f**) that the dominant decrease of the *a*-axis parameter occurred

during the early stage of Na^+ deintercalation. Upon discharging to 3.0 V (x = 0.4 in $Na_x[Mg_{0.2}Mn_{0.8}]O_2$), both the Mn–O and Mn–M distances slightly increased due to the changes in the lattice oxygen environment, below which evident changes in both the Mn–O and Mn–M distances were observed due to the reduction of Mn^{4+} toward Mn^{3+} . For NMRM, the variation of the Mn–O and Mn–M distances were slightly more visible due to the higher degree of Mn-redox participation ($Mn^{3.66+}/Mn^{4+}$) on charge. On discharge, the process was reversible with the Mn–O and Mn–M distances increased as a result of reduction from Mn^{4+} to Mn^{3+} . For the Ru K-edge EXAFS spectra, a small change was observed in the distance of Ru–O and Ru–M during the charge (**Figure 2f**). However, these distances varied much more as sodiation progressed, verifying the activity of Ru^{5+} to Ru^{4+} and further toward Ru^{3+} .

To clearly observe and determine the activity of oxygen for the NMM and NMRM electrodes, ex-situ Mg and O K-edge XANES and operando DEMS measurements were performed. The Mg and O K-edge spectra were collected under total fluorescence yield (TFY) mode for the fresh, charged (4.5 V), and discharged (1.5 V) electrodes (Figure 2g-j). The Mg K-edge spectra consisted of two major peaks at ~1306 (A) and ~1312 (B) eV for all the electrodes (Figure 2g and 2h), which is in good agreement with previous XANES results^{21,22}. However, the XANES spectra of the charged NMM and NMRM electrodes showed different peak intensity ratios, demonstrating that the coordination environment of the two systems differed. Notably, for the charged electrodes, the peak position "A" of NMM shifted toward lower photon energy; however, it did not return to the original position after discharge (Figure 2g). This result indicates the notable changes in the coordination environment around Mg atoms during charge to 4.5 V. In contrast, the NMRM electrode showed recovery of the peak position after discharging to 1.5 V (Figure 2h), implying that such coordination changes around Mg ions were suppressed by the presence of the covalent Ru–O bond in the TM layers of NMRM. In the O K-edge spectra, the two peaks appearing at ~529.5 and ~531 eV correspond to the transition of the O 1s state to the hybridized state of O 2p with 3d/4d TM of t_{2g} and e_{g} orbitals

(colored regions), respectively (**Figure 2i and 2j**). For the charged state of NMM, the intensity between the t_{2g} and e_{g} peaks increased (**Figure 2i**). The increase is attributed to the emergence of the shoulder peak at 529.8 eV, which belongs to the $(O_2)^{n-}$ peak, associated with the oxidation of O^{2-} to $(O_2)^{n-}$ as well as 1s-2p hybridization, but disappeared after discharge to 1.5 V. In contrast, there was a smaller increase in the shoulder peak after charge to 4.5 V for the NMRM (**Figure 2j**). Upon discharge to 1.5 V, the shoulder peak disappeared, and the resulting spectra recovered to the fresh state.

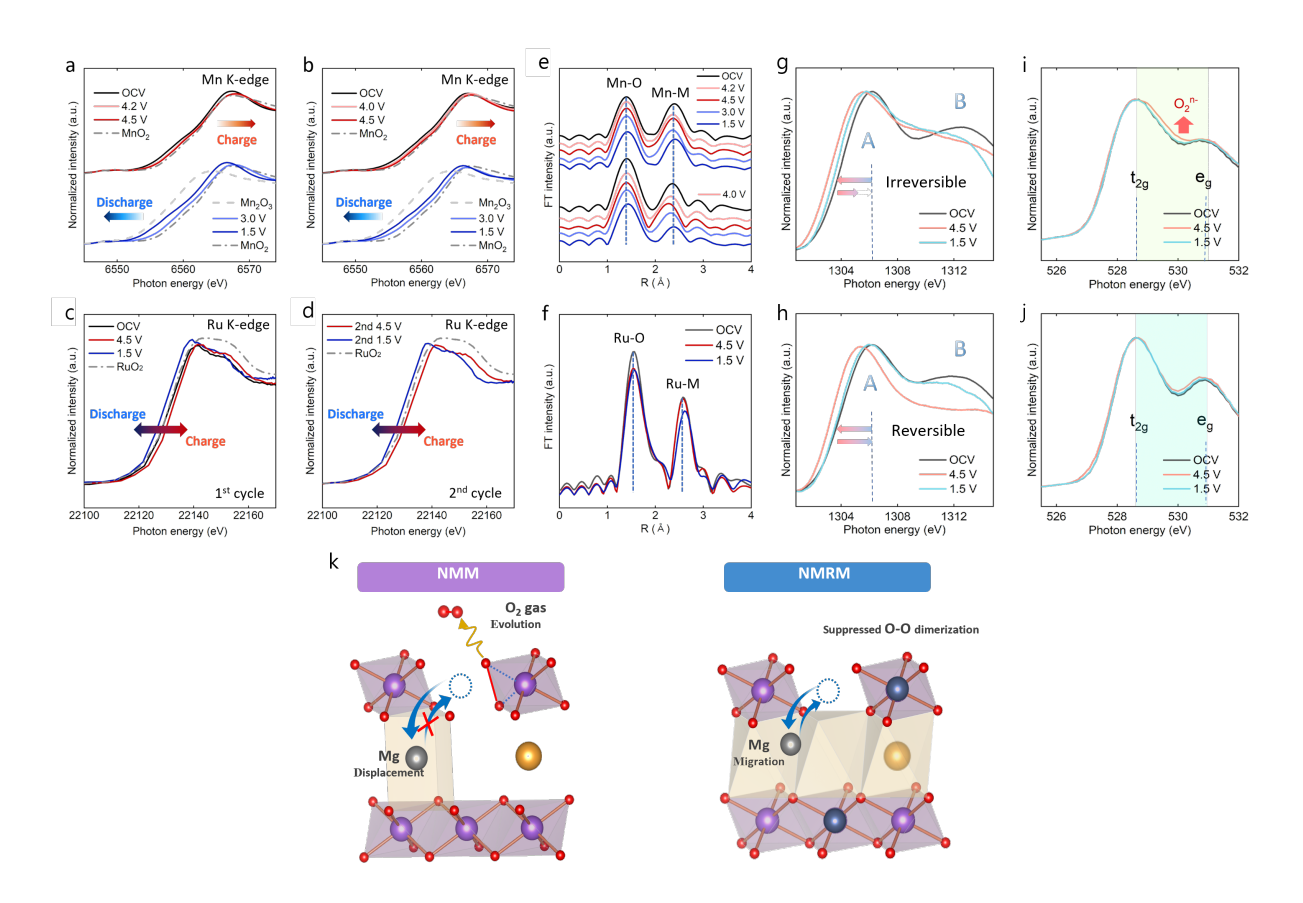


Figure 2. XANES spectra of Mn K-edge for (a) NMM and (b) NMRM; Ru K-edge of NMRM after (c) the first and (d) second cycle; EXAFS spectra of (e) Mn (top: NMM, bottom: NMRM) and (f) Ru; XANES spectra of Mg K-edge for (g) NMM and (h) NMRM; O K-edge for (i) NMM and (j) NMRM; (k) illustration for O and Mg behavior in the structure.

Complimentary insights into the effect of Ru introduction on O_2 evolution were obtained using *operando*-DEMS (**Figure S8a and S8b**). The CO₂ and O₂ evolutions were monitored in the NMM and NMRM electrodes during charge/discharge process. The NMRM electrode showed greatly diminished release of CO₂ and almost no release of O₂ gas (**Figure S8b**), which is in good agreement with the suppression of the formation of oxidized species as $(O_2)^{n-}$ for the charged NMRM electrode in the O K-edge XANES spectra (**Figure 2j**). The O₂ evolution around Mg atoms in NMM electrodes hindered reversible Na migration from the Na layer to TM sites on discharge, further leading to blockage of Na pathways and increasing the voltage hysteresis between charge and discharge (**Figure 1a**). However, Ru incorporation in NMRM enhanced covalency and prevented irreversible O₂ loss (**Figure S8b**). Therefore, as shown in **Figures S8c, S8d, S9 and S10**, higher D_{Na+} for the NMRM electrode resulted in the improved rate performance (**Figure S4d**).

To further explore local structures and Mg displacement in NMM and NMRM materials (**Figure 2k**), atomic-resolution scanning transmission electron microscopy (STEM) was employed at pristine, charged, and discharged states (**Figure 3**). The pristine NMM particle shows the layered structure composed of heavy-metal ions along the [100] zone-axis, as shown in the high-angle annular dark-field (HAADF)-STEM image in **Figure 3a**. Moreover, the magnified atomic image (**Figure 3a**, green dashed area) clearly indicates the coordination of the P2 layered structure with a uniform interlayer distance of ~5.6 Å, which is consistent with the XRD results. After charging to 4.5 V, there was a local environment change, which is most likely caused by Mg²⁺ migration out of the (001) plane (**Figure 3b and S11**). It is evident that Mg²⁺ still remained in the Na layer even after discharge to 1.5 V (**Figure 3c**). These results are in agreement with the Mg K- and O K-edge XANES spectra and *o*-DEMS, which showed irreversible Mg local structural change due to Mg displacement and the formation of O–O dimers triggered by the O₂ gas release (**Figure 2g, 2i, and S8a**). The STEM image of the fresh NMRM sample shows that it crystallizes in the same P2 crystal structure as NMM with a slight

increase in the interlayer distance ($\sim 0.91\%$) between TM layers due to the larger ionic radius of Ru⁴⁺ compared with that of Mn⁴⁺ (**Figure 3d**). Na⁺ extraction to 4.5 V led to the phase transition toward the OP4 phase with alternating octahedral and prismatic layers with interlayer distances of \sim 4.8 Å and \sim 5.5 Å, respectively (**Figure 3e and S12**). Moreover, a small portion of Mg²⁺ migrated into the O-type slabs of NMRM (**Figure 3e**). As Na⁺ is reinserted back into the NMRM structure, the P2 stacking sequence was restored with a slight observed distortion due to the formation of the P2/P'2 structure (**Figure 3f**). The structural transition from the P2 to P2/P'2 system is caused by the high level of sodium insertion into the structure, which results from the distortion of MnO₆ octahedra originating from the Jahn–Teller effect (**Figure 3f**).

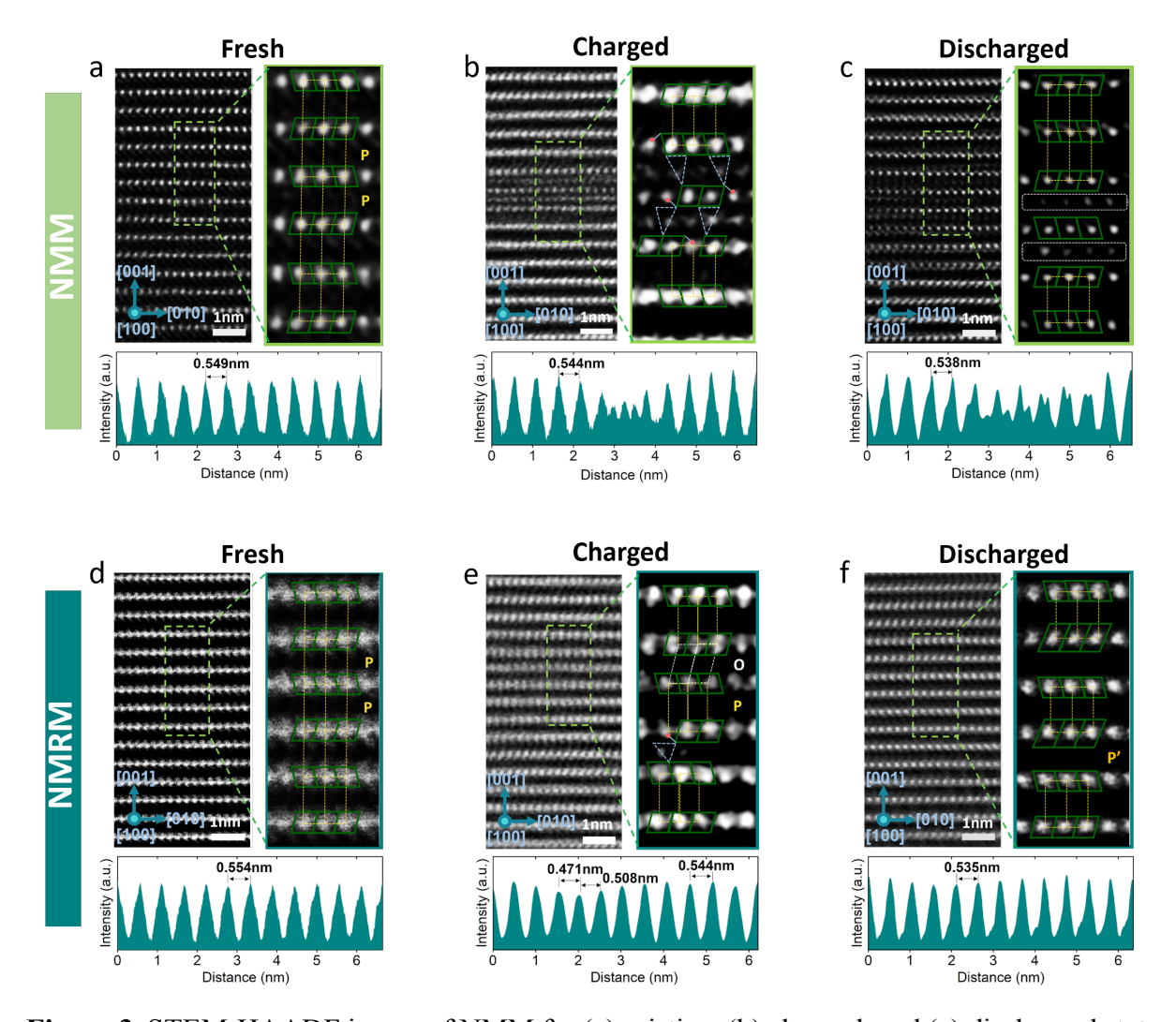


Figure 3. STEM-HAADF image of NMM for (a) pristine, (b) charged, and (c) discharged state and NMRM for (d) pristine, (e) charged, and (f) discharged state.

The computed atomistic structures of Na_xMg_{0.19}Mn_{0.81}O₂ (NMM) and Na_xMg_{0.19}Ru_{0.19}Mn_{0.62}O₂ (NMRM) with high and low concentrations of Na as well as without and with Mg migration are illustrated in **Figure 4a**. Our DFT calculations (**Figure 4a**) show that the P2 phase is stable for both high (x=0.81) and low (x=0.125) Na concentrations in the Na_xMg_{0.19}Mn_{0.81}O₂ (NMM) system. The Ru doping-induced increase in the lattice parameters of NMM is attributed to the larger ionic radii of Ru³⁺ (0.82 Å) and Ru⁴⁺ (0.76 Å) compared with those of Mn³⁺ (0.72 Å) and Mn⁴⁺ (0.67 Å). For the NMRM system, the OP4 structure is more favorable than P2 after desodiation. To understand the charge/discharge process, we characterized the redox mechanism by computing the number of unpaired electrons (N_{unp}) on ions, which represent the magnetic moment. To investigate the effect of desodiation on $N_{\rm unp}$, we first focused on model I (see SI for more details) in Figure 4b. For Na_{0.81}Mg_{0.19}Mn_{0.81}O₂ (Na₁₃Mg₃Mn₁₃O₃₂), the computed average value of $N_{\rm unp}$ ($\overline{N_{\rm unp}}$) on all the Mn cations is \approx 2.9, showing a charge of \approx 3.9+. The computed charge on O anions is \approx 2.0-. Upon a desodiation of x=0.81 \rightarrow 0.125, the calculated $\overline{N_{\rm unp}}$ for all Mn cations becomes ≈ 3.0 , indicating that the Mn oxidation state is \approx 4.0+. Some oxygen anions (e.g., number 2 in **Figure 4b**), which are close to Mg at the TM sites, are significantly oxidized by the desodiation. In the Na_{0.94}Mg_{0.19}Ru_{0.19}Mn_{0.62}O₂ $(Na_{15}Mg_3Ru_3Mn_{10}O_{32})$ system, the calculated value of $\overline{\textit{N}_{unp}}$ for Mn cations is 3.6, indicating a charge of $\approx 3.4+$ on Mn. The predicted average charge on Ru ($\overline{N_{\rm unp}}$ =1.1) cations is $\approx 3.1+$. The low charge state of Ru is forced by the large number of accommodated Na (Na_{0.94}) in the discharged state. This phenomenon might indicate that the reduction of Mn to 3+ is less favorable compared with that of Ru. One of the reasons for the high capacity of the Ru-doped system is the high tendency for the reduction of Ru. For the Ru-doped system, with the desodiation of $x=0.94 \rightarrow 0.125$, all the Mn cations have a charge state of $\approx 4.0 + (\overline{N_{\rm unp}} = \approx 3.0)$. The desodiation-induced oxidation of Ru depends on the position of Ru cation at TM sites. When a single Ru cation exists at each TM layer in the supercell (i.e., the nearest neighbors of Ru are Mn), it experiences almost a full oxidation from 3.1+ to 4.1+ $(\overline{N_{\rm unp}}=1.1 \rightarrow 2.1)$. However, when Ru cations are nearest neighbors, they undergo a smaller oxidation from 3.1+ to 3.5+ $(\overline{N_{\rm unp}}=1.1\rightarrow1.5)$, which is probably due to the strong overlap of d orbitals of Ru cations with p orbitals of O anions and those of their nearest neighbors. As a larger (desodiationinduced) oxidation of Ru is observed in our experimental XANES results (Figure 2c and 2d) compared to our calculations, we concluded that the Ru cations should be homogeneously distributed in TM layers and not clustered in the O-TM-O layer. To confirm this conclusion and investigate the influence of Hartree-Fock HF mixing constant on TM charges we studied model II (Figure 4b, see SI for more details). It is found that the average desodiation-induced oxidation of Mn in the NMM system $(3.5+\rightarrow 3.9+)$ is similar to that in the NMRM one $(3.5+\rightarrow 3.9+)$. The average oxidation of O in the NMM system is, however, larger (+0.24 for NMM and +0.11 for NMRM); however, both Ru cations in the NMRM supercell are very active compared to Mn cations and O anions. The average oxidation of Ru cations due to the desodiation of $x=0.875\rightarrow0.125$ is 1.27. Half of the Ru cations oxidize to $\approx4.3+$, which is the highest value that we obtained from DFT calculation. The oxidation state of both Ru and Mn can slightly change with the value of the HF mixing constant of the HSE06 functional. The computed value of $N_{\rm unp}$ for Ru and Mn with the value of α =0.35 appears to be closer to the experiment. The computed average oxidation state of Ru in model II (4.1+) agrees better with our experimental XANES data (Figure 2c and 2d) in comparison to Model I (3.7+). This confirms our hypothesis that Ru cations do not occupy nearest-neighbor sites at TM layer, which can be understood by the unfavorable repulsive interaction between strongly oxidized Ru cations that would occupy nearest-neighbor sites. However, we find that the Mg migration to Na sites (model II), which leaves behind vacant sites in the TM layer, cannot greatly increase the oxidation state of Ru as this value is even lower in the sodiated case of Model II compared with that in Model I.

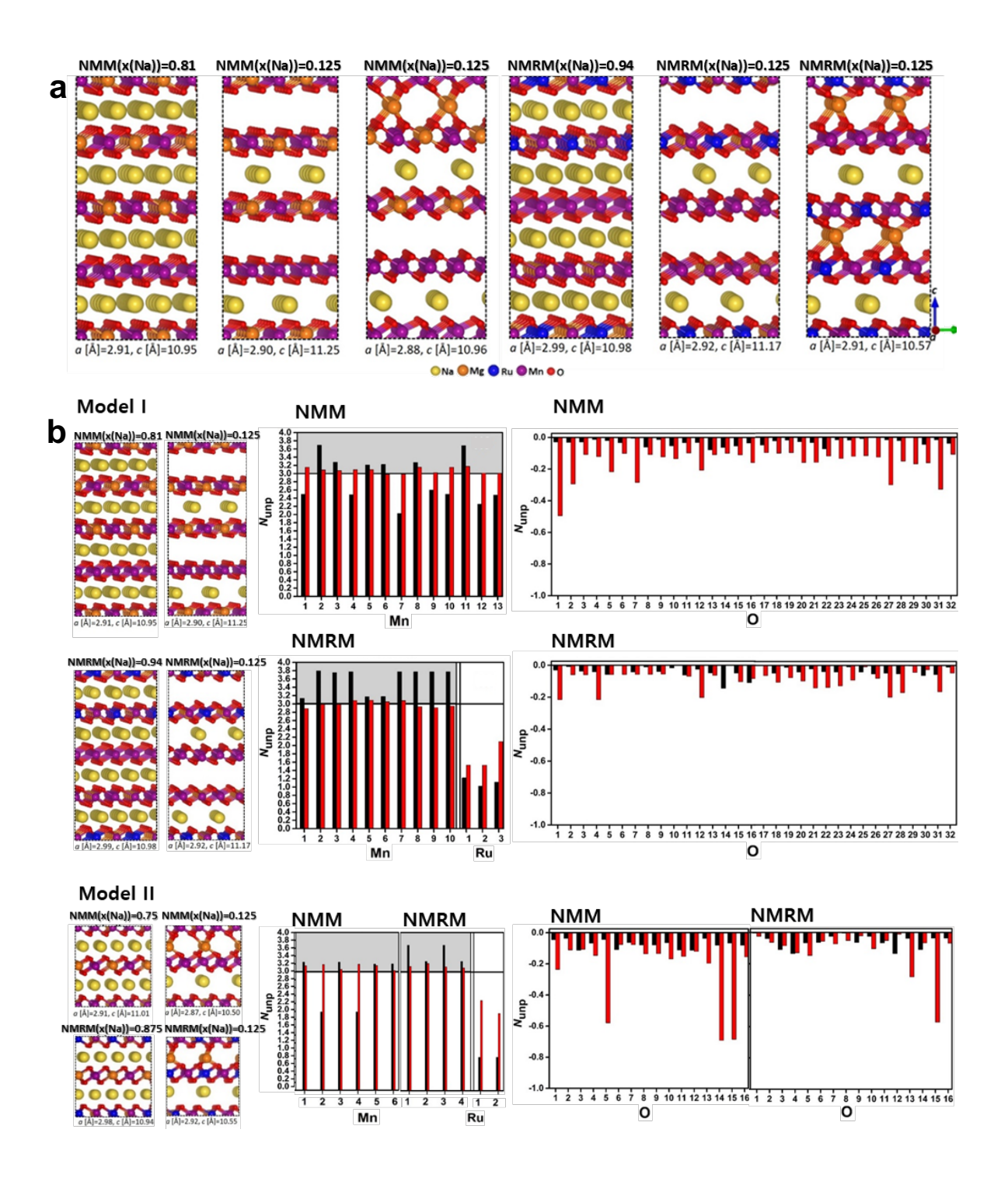


Figure 4. (a) Computed atomistic structures of NMM and NMRM at high and low Naconcentrations; (b) Calculated atomistic structures and $N_{\rm unp}$ of ions for Model I) Na_xMg_{0.19}Mn_{0.81}O₂ (NMM) and Na_xMg_{0.19}Ru_{0.19}Mn_{0.62}O₂ (NMRM) at high and low Naconcentrations without Mg migration using a Hartree-Fock mixing constant of 0.25 as well as model II) Na_xMg_{0.25}Mn_{0.75}O₂ (NMM) and Na_xMg_{0.25}Ru_{0.25}Mn_{0.5}O₂ (NMRM) at high and low Naconcentrations with Mg migration using a Hartree-Fock mixing constant of 0.35. The grey shaded region shows Mn with high spin.

Ru incorporation into the TM layer instead of Mn balances the cationic and anionic redox participation and, as a result, delivers higher capacity. The charge compensation in Ru-free Na_{0.6}[Mg_{0.2}Mn_{0.8}]O₂ is progressed by O²⁻/(O₂)ⁿ⁻ and Mn³⁺/Mn⁴⁺ redox couples in approximately equal proportions. In the Ru-assisted one, TM redox pairs, such as Ru³⁺/Ru⁴⁺/Ru⁵⁺ and Mn³⁺/Mn⁴⁺, are more dominant. Ru, which increases the covalency with oxygen, adjusts the degree of O²⁻/(O₂)ⁿ⁻ redox participation and not only suppresses the oxygen release but also diminishes the voltage hysteresis in the Na_{0.6}[Mg_{0.2}Ru_{0.2}Mn_{0.6}]O₂ material. Moreover, the presence of the higher-covalency Ru–O bond minimizes Mg migration from the TM to Na layers during charge, promoting reversibility of the redox reactions and structural stabilization for long-term (**Figure S13**).

ASSOCIATED CONTENT

Supporting Information

The Supporting Information is available free charge https://pubs.acs.org/doi/10.1021/acsenergylettXXXXX. **Synthesis** and characterization, crystal structures, XRD, Rietveld refinement, TEM, SEM, ICP AES, particle size distribution, electrochemical performance, o-XRD patterns and corresponding lattice parameters, ex situ XANES Mn K edge, Ru K edge, O K edge, o-DEMS, GITT and corresponding calculated Na⁺ diffusion coefficients, STEM-HAADF images, o-XRD patterns after 200 cycled NMRM, and computational details (Figure S1 – **S13, Table S1-S6**). (MS Word)

AUTHOR INFORMATION

Corresponding Authors

Payam Kaghazchi – Forschungszentrum Jülich GmbH, Institute of Energy and Climate Research, Materials Synthesis and Processing (IEK-1), Jülich, 52428, Germany; MESA+

Institute for Nanotechnology, University of Twente, 7500 AE Enschede, the Netherlands; Email: p.kaghazchi@fz-juelich.de

Seung-Taek Myung – Hybrid Materials Research Center, Department of Nano Technology and Advanced Materials Engineering, Sejong Battery Institute, Sejong University, Seoul 05006, South Korea; Email: smyung@sejong.ac.kr

Authors

Jun Ho Yu – Hybrid Materials Research Center, Department of Nano Technology and Advanced Materials Engineering, Sejong Battery Institute, Sejong University, Seoul 05006, South Korea

Natalia Voronina – Hybrid Materials Research Center, Department of Nano Technology and Advanced Materials Engineering, Sejong Battery Institute, Sejong University, Seoul 05006, South Korea

Najma Yaqoob – Forschungszentrum Jülich GmbH, Institute of Energy and Climate Research, Materials Synthesis and Processing (IEK-1), Jülich, 52428, Germany; MESA+ Institute for Nanotechnology, University of Twente, 7500 AE Enschede, the Netherlands

Sungkyu Kim – Hybrid Materials Research Center, Department of Nano Technology and Advanced Materials Engineering, Sejong Battery Institute, Sejong University, Seoul 05006, South Korea

Anil Kumar Paidi – Pohang Accelerator Laboratory, 80 Jigokro-127-beongil, Nam-gu, Pohang, Gyeongbuk 37673, South Korea

Docheon Ahn – Pohang Accelerator Laboratory, 80 Jigokro-127-beongil, Nam-gu, Pohang, Gyeongbuk 37673, South Korea

Kyuwook Ihm – Pohang Accelerator Laboratory, 80 Jigokro-127-beongil, Nam-gu, Pohang, Gyeongbuk 37673, South Korea

Keun Hwa Chae – Pohang Accelerator Laboratory, 80 Jigokro-127-beongil, Nam-gu, Pohang, Gyeongbuk 37673, South Korea; Center for Energy Storage Research, Korea Institute of Science and Technology, Seoul 02792, South Korea

Min-Gi Jeong – Center for Energy Storage Research, Korea Institute of Science and Technology, Seoul 02792, South Korea

Hun-Gi Jung – Center for Energy Storage Research, Korea Institute of Science and Technology, Seoul 02792, South Korea; KIST-SKKU Carbon-Neutral Research Center, Sungkyunkwan University, Suwon 16419, South Korea; Department of Energy Science, Sungkyunkwan University, Suwon 16419, South Korea

Olivier Guillon – Forschungszentrum Jülich GmbH, Institute of Energy and Climate Research, Materials Synthesis and Processing (IEK-1), Jülich, 52428, Germany

Author Contributions

J. H. Yu and N. Voronina contributed equally. The manuscript was written through the contributions of all authors. All authors have given approval to the final version of the

manuscript. J.H.Y., N.V., P.K., and S.-T.M developed the concept of the work and the whole content, and wrote the manuscript with all authors. S.K. performed TEM observation, and XAS experiments were assisted by A.K.P., D.A., I.K., and C.K.H.. *O*-DEMS observation was performed by M.-G.J. and H.-G.J.. Simulation was led by N.Y., O.G., and P.K.

Notes

The authors declare no competing financial interests.

Acknowledgements

This work was supported by the Basic Science Research Program through the National Research Foundation of Korea (NRF), funded by the Ministry of Education, Science, and Technology of Korea (NRF-2020R1A6A1A03043435, NRF-2022M3H4A1A04096478, NRF-2023R1A2C2003210, NRF-2022R1F1A1063351). This research was also supported by Technology Innovation Program (Alchemist Project, 20012196, AI based supercritical materials discovery) funded by the Ministry of Trade, Industry and Energy, Korea. P. K. gratefully acknowledges support from the "Bundesministerium für Bildung und Forschung" (BMBF) and the computing time granted through JARA-HPC on the supercomputer JURECA at Forschungszentrum Jülich.

References

- (1) Nitta, N.; Wu, F.; Lee, J. T.; Yushin, G. Li-Ion Battery Materials: Present and Future. *Mat. Today.* **2015**, *18* (5), 252–264. https://doi.org/10.1016/j.mattod.2014.10.040.
- (2) Ohzuku, T.; Nagayama, M.; Tsuji, K.; Ariyoshi, K. High-Capacity Lithium Insertion Materials of Lithium Nickel Manganese Oxides for Advanced Lithium-Ion Batteries: Toward Rechargeable Capacity More than 300 mAh g⁻¹. *J. Mater. Chem.* **2011**, *21* (27), 10179–10188. https://doi.org/10.1039/c0jm04325g.
- (3) Thackeray, M. M.; Wolverton, C.; Isaacs, E. D. Electrical Energy Storage for Transportation Approaching the Limits of, and Going beyond, Lithium-Ion Batteries. *Energy & Environ. Sci.* **2012**, *5*, 7854–7863. https://doi.org/10.1039/c2ee21892e.

- (4) Rozier, P.; Tarascon, J. M. Review—Li-Rich Layered Oxide Cathodes for Next-Generation Li-Ion Batteries: Chances and Challenges. *J. Electrochem. Soc.* **2015**, *162* (14), A2490–A2499. https://doi.org/10.1149/2.0111514jes.
- Voronina, N.; Sun, Y. K.; Myung, S. T. Co-Free Layered Cathode Materials for High Energy Density Lithium-Ion Batteries. *ACS Energy Lett.* **2020**, *5*, 1814–1824. https://doi.org/10.1021/acsenergylett.0c00742.
- (6) Vaalma, C.; Buchholz, D.; Weil, M.; Passerini, S. A cost and resource analysis of sodium-ion batteries. *Nat. Rev. Mater.* **2018**, *3*, 18013. https://doi.org/10.1038/natrevmats.2018.13
- (7) Voronina, N.; Yu, J. H.; Kim, H. J.; Yaqoob, N.; Guillon, O.; Kim, H.; Jung, M. G.; Jung, H. G.; Yazawa, K.; Yashiro, H.; Kaghazchi, P.; Myung, S. T. Engineering Transition Metal Layers for Long Lasting Anionic Redox in Layered Sodium Manganese Oxide. *Adv. Funct. Mater.* **2023**, *33*, 2210423. https://doi.org/10.1002/adfm.202210423.
- (8) Hwang, J. Y.; Myung, S. T.; Sun, Y. K. Sodium-Ion Batteries: Present and Future. *Chem. Soc. Rev.* **2017**, *46*, 3529–3614. https://doi.org/10.1039/c6cs00776g.
- (9) De La Llave, E.; Talaie, E.; Levi, E.; Nayak, P. K.; Dixit, M.; Rao, P. T.; Hartmann, P.; Chesneau, F.; Major, D. T.; Greenstein, M.; Aurbach, D.; Nazar, L. F. Improving Energy Density and Structural Stability of Manganese Oxide Cathodes for Na-Ion Batteries by Structural Lithium Substitution. *Chem. Mater.* **2016**, *28* (24), 9064–9076. https://doi.org/10.1021/acs.chemmater.6b04078.
- (10) Zhao, C.; Li, C.; Liu, H.; Qiu, Q.; Geng, F.; Shen, M.; Tong, W.; Li, J.; Hu, B. Coexistence of $(O_2)^{n-1}$ and Trapped Molecular O_2 as the Oxidized Species in P2-Type Sodium 3*d* Layered Oxide and Stable Interface Enabled by Highly Fluorinated Electrolyte. *J. Am. Chem. Soc.* **2021**, *143* (44), 18652–18664. https://doi.org/10.1021/jacs.1c08614.
- (11) House, R. A.; Maitra, U.; Pérez-Osorio, M. A.; Lozano, J. G.; Jin, L.; Somerville, J. W.; Duda, L. C.; Nag, A.; Walters, A.; Zhou, K. J.; Roberts, M. R.; Bruce, P. G. Superstructure Control of First-Cycle Voltage Hysteresis in Oxygen-Redox Cathodes. *Nature* **2020**, *577* (7791), 502–508. https://doi.org/10.1038/s41586-019-1854-3.
- (12) Voronina, N.; Shin, M. Y.; Kim, H. J.; Yaqoob, N.; Guillon, O.; Song, S. H.; Kim, H.; Lim, H. D.; Jung, H. G.; Kim, Y.; Lee, H. K.; Lee, K. S.; Yazawa, K.; Gotoh, K.; Kaghazchi, P.; Myung, S. T. Hysteresis-Suppressed Reversible Oxygen-Redox Cathodes for Sodium-Ion Batteries. *Adv Energy Mater* 2022, *12*, 2103939. https://doi.org/10.1002/aenm.202103939.
- (13) Clément, R. J.; Billaud, J.; Robert Armstrong, A.; Singh, G.; Rojo, T.; Bruce, P. G.; Grey, C. P. Structurally Stable Mg-Doped P2-Na_{2/3}Mn_{1-Y}Mg_yO₂ Sodium-Ion Battery Cathodes with High Rate Performance: Insights from Electrochemical, NMR and Diffraction Studies. *Energy & Environ. Sci.* **2016**, *9*, 3240–3251. https://doi.org/10.1039/c6ee01750a.
- (14) Maitra, U.; House, R. A.; Somerville, J. W.; Tapia-Ruiz, N.; Lozano, J. G.; Guerrini, N.; Hao, R.; Luo, K.; Jin, L.; Pérez-Osorio, M. A.; Massel, F.; Pickup, D. M.; Ramos, S.; Lu, X.; McNally, D. E.; Chadwick, A. V.; Giustino, F.; Schmitt, T.; Duda, L. C.; Roberts, M. R.; Bruce, P. G. Oxygen Redox Chemistry without Excess Alkali-Metal Ions in Na_{2/3} [Mg_{0.28}Mn_{0.72}]O₂. Nat. Chem. 2018, 10 (3), 288–295. https://doi.org/10.1038/nchem.2923.
- (15) Boivin, E.; House, R. A.; Pérez-Osorio, M. A.; Marie, J. J.; Maitra, U.; Rees, G. J.; Bruce, P. G. Bulk O₂ Formation and Mg Displacement Explain O-Redox in Na_{0.67}Mn_{0.72}Mg_{0.28}O₂. *Joule* **2021**, *5* (5), 1267–1280. https://doi.org/10.1016/j.joule.2021.04.006.
- (16) Bassey, E. N.; Reeves, P. J.; Jones, M. A.; Lee, J.; Seymour, I. D.; Cibin, G.; Grey, C. P. Structural Origins of Voltage Mysteresis in the Na-Ion Cathode P2-

- Na_{0.67}[Mg_{0.28}Mn_{0.72}]O₂: A Combined Spectroscopic and Density Functional Theory Study. *Chem. Mater.* **2021**, *33* (13), 4890–4906. https://doi.org/10.1021/acs.chemmater.1c00248.
- (17) Zhao, C.; Chen, C.; Hu, B.; Tong, W.; Liu, H.; Hu, B.; Li, C. Correlating Mg Displacement with Topologically Regulated Lattice Oxygen Redox in Na-Ion Layered Oxide Cathodes. *Chem. Mater.* **2022**, *34* (20), 9240–9250. https://doi.org/10.1021/acs.chemmater.2c02474.
- (18) Bai, X.; Iadecola, A.; Tarascon, J. M.; Rozier, P. Decoupling the Effect of Vacancies and Electropositive Cations on the Anionic Redox Processes in Na Based P2-Type Layered Oxides. *Energy Storage Mater.* **2020**, *31*, 146–155. https://doi.org/10.1016/j.ensm.2020.05.032.
- (19) Yang, L.; Liu, Z.; Liu, S.; Han, M.; Zhang, Q.; Gu, L.; Li, Q.; Hu, Z.; Wang, X.; Lin, H. J.; Chen, C. Te; Chen, J. M.; Haw, S. C.; Wang, Z.; Chen, L. Superiority of Native Vacancies in Activating Anionic Redox in P2-Type Na_{2/3}[Mn_{7/9}Mg_{1/9}□_{1/9}]O₂. *Nano Energy* **2020**, *78*, 105172. https://doi.org/10.1016/j.nanoen.2020.105172.
- (20) Voronina, N.; Yaqoob, N.; Kim, H. J.; Lee, K. S.; Lim, H. D.; Jung, H. G.; Guillon, O.; Kaghazchi, P.; Myung, S. T. A New Approach to Stable Cationic and Anionic Redox Activity in O3-Layered Cathode for Sodium-Ion Batteries. *Adv Energy Mater* **2021**, *11*, 2100901. https://doi.org/10.1002/aenm.202100901.
- (21) Tuerxun, F.; Yamamoto, K.; Hattori, M.; Mandai, T.; Nakanishi, K.; Nakanishi, K.; Choudhary, A.; Tateyama, Y.; Sodeyama, K.; Nakao, A.; Uchiyama, T.; Matsui, M.; Tsuruta, K.; Tamenori, Y.; Kanamura, K.; Uchimoto, Y. Determining Factor on the Polarization Behavior of Magnesium Deposition for Magnesium Battery Anode. *ACS Appl. Mater. Interfaces* **2020**, *12* (23), 25775–25785. https://doi.org/10.1021/acsami.0c03696.
 - (22) Singh, J. P.; Kumar, M.; Chae, K. H.; Lee, I.-J. X-ray reflectivity and near edge X-ray absorption fine structure investigations of MgO thin films. *Appl. Sci. Lett.* **2017**, *3* (3), 47–52. https://doi.org/10.17571/appslett.2017.03013.